Article

Multiferroics Made via Chemical Co-Precipitation That Is Synthesized and Characterized as $Bi_{(1-x)}Cd_xFeO_3$

Syed Zain Mehmood [1,*], Mubashar Arshad [2,*], Fahad M. Alharbi [3], Sayed M. Eldin [4] and Ahmed M. Galal [5,6]

1   Department of Physics, Faculty of Sciences, University of Gujrat, Gujrat 50700, Pakistan
2   Department of Mathematics, University of Gujrat, Gujrat 50700, Pakistan
3   Department of Mathematics, Al-Qunfudah University College, Umm Al-Qura University, Mecca 24382, Saudi Arabia
4   Center of Research, Faculty of Engineering, Future University in Egypt, New Cairo 11835, Egypt
5   Department of Mechanical Engineering, College of Engineering in Wadi Alddawasir, Prince Sattam bin Abdulaziz University, Wadi Addawaser 11991, Saudi Arabia
6   Production Engineering and Mechanical Design Department, Faculty of Engineering, Mansoura University, Mansoura 35516, Egypt
*   Correspondence: szain@phys.qau.edu.pk (S.Z.M.); imbashrii@gmail.com (M.A.)

Abstract: Cd-doped $BiFeO_3$ powders, with varying doping concentrations of Cd ($Bi_{(1-x)}Cd_xFeO_3$, where x = 0–0.3), were prepared through a facile chemical co-precipitation method and calcinated at 550 °C in the air. The $BiFeO_3$ has a rhombohedral crystal structure, which changes to an orthorhombic crystal structure with an increase in Cd doping. The presence of dopant has also altered the bandgap of material suppressing it from 2.95 eV to 2.51 eV, improving the visible light absorption. Vibrating sample magnetometry (VSM) confirmed stronger ferromagnetic character for $Bi_{0.7}Cd_{0.3}FeO_3$ with a coercivity of 250 Oe, and remnant magnetization was 0.15 emu/g, which is because of the misalignment of the two sublattices of perovskite structure after doping resulting in the imbalanced magnetic moment giving rise to net nonzero magnetic behavior. The particle size reduction is observed with an increase in the doping concentration of Cd.

Keywords: multiferroics; co-precipitation method; doping concentration; structural transition; magnetic behavior; VSM

1. Introduction

In the recent past, multiferroics have attained tremendous attention from researchers because of their vital role in the manufacturing of memory storage devices, spintronics, and magneto-electric sensors [1,2]. Multiferroics are materials possessing both ferromagnetic and ferroelectric properties at the same time. Generally, a material should be a metal to show good ferromagnetic behavior, or it should be an insulator/dielectric (to become polarized) to exhibit the phenomenon of ferroelectricity. This makes multiferroics rare and valuable materials for the electronics industry [3–5]. To date, many multiferroics have been reported. The general universal formula ABX_3 represents the family of materials having a perovskite structure. Here, A and B represent the cations, and X is the anion. X can vary from oxides to halides, which means there can be an oxide element or halide group element, for example, Br, Cl, or I_2, which can be used as halides. A wide range of perovskite materials, including $BiFeO_3$, $BiMnO_3$, and $ZMnO_3$, where Z can be a rare earth metal such as Y, Tb, Ho, Lu, etc., are multiferroic. Other examples include $BaTiO_3$, which is dielectric ferroelectric and is used in multilayer ceramic capacitors and sensors. $PbTiO_3$ possesses pyroelectric and piezoelectric properties and is used in transducers for marine and underwater devices and is also used as a protector. $Na_{0.5}Bi_{0.5}$ is reported for showing ferroelectricity and is used in piezoceramics.

Among the above-mentioned multiferroics, $BiFeO_3$ is a significant compound exhibiting relatively high Neel temperature (370 °C) and Curie temperature (830 °C), which is

the main point of interest for potential applications in the industry where exposure to high temperatures [6,7]. Secondly, $BiFeO_3$ is more resistant to rust, as well. $BiFeO_3$ is a well known ferrite, and research is performed with many different doping elements, for instance, Dzik et al. [8] examined the Dy doping in the place of Bi in $BiFeO_3$ and observed the enhanced magnetic properties of the sample from 0.1 emu/g for the pure sample and 0.3 emu/g for the 10% doped sample when measured at room temperature (300 K). Dy also increased the measuring field frequency value for the sample at all temperatures. The obtained samples were in ceramic form when prepared with the mixed oxide method. Additionally, Ishaq et al. [9] investigated the effect of Mn-Cd co-doping in $BiFeO_3$ and confirmed the grain size reduction of the samples with increasing doping concentration of dopants. The structural transition of pure bismuth ferrite crystal from rhombohedral to orthorhombic occurred whenever the bismuth ferrite particles were doped with a suitable metallic element in the Bi site. Moreover, D.V. Karpinsky et al. [10] reported the maximum remnant magnetization of 0.07 emu/g for Mn and Ca co-doping in $BiFeO_3$ samples, and the antiferromagnetic behavior is observed. Arfat et al. [11] reported the specific magnetization lay around the value of 2.9 emu/g associated with 10% doping of Ni in $BiFeO_3$. This value of specific magnetization increased significantly when increasing the value of x, which is the value of the concentration of doping.

$BiFeO_3$ is a perovskite having a distorted rhombohedral structure lying in the R3c space group. It shows relatively higher electrical conductivity due to the presence of $Bi_2Fe_4O_9$ and $Bi_{25}FeO_{40}$ secondary phases [12]. The volatilization of Fe^{2+} ions and Bi^{3+} ions at high temperatures also plays a key role in the conduction of electric current. The synthesis of single-phase bismuth ferrites is very hard due to the formation of secondary phases, which simply cannot be avoided by rapid sintering [13–17]. The literature suggests that the substitution of rare earth ions or alkali earth ions, such as Y^{3+}, Nd^{3+}, Sm^{3+}, Sr^{2+}, and Ba^{2+} can improve some properties, including magnetic and electric properties of $BiFeO_3$ [18–20]. Further, the reduction in the leakage current can be achieved by suppressing the spiral structure of $BiFeO_3$ perovskite and reducing its particle size [21–23].

Bismuth causes space charge defects (such as oxygen vacancies) in the perovskite structure. These free-to-move charges gather at lower energy places (such as ferroelectric domain walls) or grain boundaries when an external electric field is applied [24]. Consequently, $BiFeO_3$ leakage current (due to secondary phases) and oxygen vacancies limit the ferroelectric loop by gathering on the domain walls. This sets up a limit for multiferroics to be efficiently used in magneto-electric devices [25–27]. The Fe^{3+} ions (partially filling the 3d orbital) are the main cause of G-type antiferromagnetic ordering, resulting from the Jahn Teller effect during structure distortion of the bulk $BiFeO_3$ [28,29].

Generally, $BiFeO_3$ can be synthesized by several methods, such as the solid-state method, sol-gel process, hydrothermal technique, and chemical co-precipitation method. In the solid-state method, precursors are manually mixed, and nitric acid is mostly used for leaching to avoid the impurity phases [30–32]. Similarly, leaching methods are also used in the sol-gel route to form ceramics of $BiFeO_3$. $BiFeO_3$ samples with Cd doping yield a relatively low number of undesired secondary phases (responsible for poor electrical and magnetic properties) in multiferroics. A lower quantity of undesired secondary phases of the final product is the main concern leading towards particularly selecting the chemical coprecipitation method [33–36]. Based upon the requirement of the final powder, several synthesis routes have been adopted by different researchers to produce $BiFeO_3$. Among these methods, some are suitable to achieve small particles size, while others are useful to produce a powder with high purity levels [37,38]. The particle size of a material can have a significant influence on its magnetic behavior. In general, as the particle size decreases, the magnetic properties of the material tend to become more pronounced. This is due to the increased surface-to-volume ratio of smaller particles, which leads to a higher density of surface defects and an increased number of unpaired electrons on the surface. These factors can lead to a higher susceptibility to magnetic fields and a greater overall magnetic moment.

For ferromagnetic materials, as the particle size decreases, the Curie temperature (Tc) tends to decrease, which means that ferromagnetic ordering can occur at lower temperatures. Additionally, the coercive field (Hc) tends to increase, meaning that it takes a stronger magnetic field to switch the magnetization direction.

In addition, it is also important to consider the shape of the particles as well. Spherical particles will have different magnetic properties than elongated particles of the same size. It is worth noting that the particle size effect on magnetic behavior is not always linear, and sometimes more complex relations can be observed. Preparation of $BiFeO_3$ particles can also be achieved using the hydrothermal method, but the resulting particle size is sometimes larger than several hundred nanometers. Preparation of $BiFeO_3$ nano-crystals at elevated temperatures (up to 200 °C) using KOH as precipitating agent is reported by Chen et al. [39]. Conventional synthesis routes for preparing $BiFeO_3$ particles generally involve the mixing of precursors in stoichiometric amounts, and the reaction rate largely depends upon the particle size and temperature. Chemical co-precipitation, on the other hand, is a well known method for obtaining particles with relatively smaller sizes and higher degrees of homogenization. Further, this technique does not involve very high temperatures or heavy apparatus, while many physical properties of the powder can be modified by controlling the external conditions, such as temperature, stirring period, stirring speed, amount, and type of precipitating agent. The volatilization of both Fe^{2+} ions and Bi^{3+} ions at high temperatures can play a key role in the conduction of electric current in $BiFeO_3$. However, it is true that, in some studies, the problem of Bi volatilization during synthesis is emphasized, but the volatilization of Fe ions is not mentioned. This is likely because the volatilization of Bi ions is more pronounced and can have a greater impact on the properties of the final material. Additionally, the OZDEMIR methods [40] used to prevent Bi volatilization, such as using a reducing atmosphere or low-temperature synthesis, may also help to reduce the volatilization of Fe ions.

Therefore, in this work, a simple, facile, and efficient chemical co-precipitation technique was successfully used to synthesize $BiFeO_3$ with different doping concentrations of Cd ($Bi_{1-x}Cd_xFeO_3$, where x = 0, 0.1, 0.3). The electrical, magnetic, optical, and structural properties of the ferrites were systematically studied through vibrating sample magnetometry, X-ray diffraction, scanning electron microscopy, EDX analysis, ultraviolet-visible spectroscopy, and Raman spectroscopy.
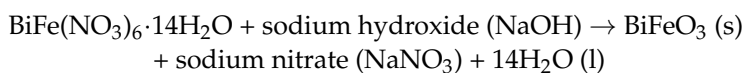
2. Experimental Procedure

$Bi_{1-x}Cd_xFeO_3$ (x = 0, 0.1, 0.3) samples were prepared via a simple chemical co-precipitation method using high-purity (<99%) precursors. The nitrates of metallic salts [$Bi(NO_3)_3\cdot5H_2O$, $Cd(NO_3)_2\cdot4H_2O$, $Fe(NO_3)_3\cdot9H_2O$] were used in their as-received state with no further processing. All precursors (in the stoichiometric amount) were mixed in deionized water at room temperature. The initial solution of each nitrate was stirred up until it was completely dissolved. After preparing the solutions of each reagent, they were mixed in a beaker under continuous stirring, and the temperature of the solution was slightly elevated to 60 °C. Nitric acid and polyethylene glycol (PEG) were added dropwise in a small ratio to control the morphology of particles. Further, nitric acid was used as a bleaching agent to avoid nucleation of impurity phases. Subsequently, ammonia solution was added dropwise to settle down the particles in the beaker. The whole process was carried out under constant stirring for 3 h without reducing the temperature. Finally, the prepared ferrite particles were allowed to settle down at room temperature and washed three to four times with deionized water. The pH of the resulting liquid precursor was kept between 7–9 with the help of ammonia solution and washing process. The resulting solution was then dried in an oven maintained at 80 °C. Finally, all dried powder precursors were calcined at 550 °C for 3 h in air. The final product was then ground to obtain a homogenous fluffy powder.

The co-precipitation synthesis of $BiFeO_3$ nanoparticles can be represented by the following chemical reaction equations:

- Formation of metal precursors:

Bismuth nitrate pentahydrate ($Bi(NO_3)_3 \cdot 5H_2O$) + iron nitrate nonahydrate ($Fe(NO_3)_3 \cdot 9H_2O$) $\rightarrow$ bismuth iron nitrate hexahydrate ($BiFe(NO_3)_6 \cdot 14H_2O$)

- Precipitation of metal oxides:

$$BiFe(NO_3)_6 \cdot 14H_2O + \text{sodium hydroxide (NaOH)} \rightarrow BiFeO_3 \text{ (s)}$$
$$+ \text{sodium nitrate } (NaNO_3) + 14H_2O \text{ (l)}$$

- Calcination of metal oxides:

$$BiFeO_3 \text{ (s)} \rightarrow BiFeO_3 \text{ (s) (calcined)}$$

The calcination step is usually performed at high temperatures (e.g., 500–600 °C) to remove any residual water and to obtain crystalline $BiFeO_3$ nanoparticles.

The structural and morphological characteristics of the prepared samples were revealed by X-ray diffraction using the GNR EXPLORER 2000 (XRD) and the scanning electron microscope TESCAN MAIA3 (SEM), respectively. The XRD was carried out using Cu-Kα radiations (with wavelength 1.54 Å) in the 2-theta range of 20–60°. To study the magnetic properties of the prepared powders, vibrating sample magnetometry (VSM) (Lake Shore 7300) was performed. Moreover, ultraviolet-visible UV1800 (UV) spectroscopy and Raman spectroscopy DPSSL laser source (with lambda = 532 nm/150 mW), as an excitation source (RS), were performed to study the absorption peaks/band gap, as well as the emission spectra of the prepared samples. Fourier transform-infrared spectroscopy FT/IR-4100 type-A, JASCO (FT-IR) was performed to analyze the bonding of oxygen with cations and the effect of doping on bonding.

3. Results and Discussion

3.1. X-ray Diffraction

Figure 1 shows the XRD patterns of $BiFeO_3$, $Bi_{0.9}Cd_{0.1}FeO_3$, and $Bi_{0.7}Cd_{0.3}FeO_3$ compounds, which were calcined at 550 °C for 3 h in the powder form. The XRD pattern confirms the rhombohedral structure of the $BiFeO_3$ sample that belongs to the R3c space group. Interestingly, no secondary phase of bismuth ferrite was found in the pure sample. The main peak is observed at 2-theta ~32°, which corresponds to 110 crystallographic planes. After the substitution of Cd in $BiFeO_3$, a structural transition from rhombohedral to orthorhombic is observed, as shown in Figure 1, showing the characteristic dual peaks near ~32°, which are attributed to the orthorhombic phase. The peaks at 2-theta ~46° and ~53° splits into two sub-peaks, and the main peak with the highest intensity tends to broaden, which confirms the successful substitution of Cd with Bi in $BiFeO_3$. This broadening of peaks increases with the increase in Cd doping. This might be associated with the fact that the ionic radii of Bi and Cd are different. The ionic radius of Cd^{+2} is 95 pm and has a smaller ionic radius than that of Bi^{+2}, which is 116 pm under the same conditions. Therefore, a transition from rhombohedral to the orthorhombic type of structure took place. Moreover, the $Bi_2Fe_4O_9$ impurity phase and $Bi_{25}FeO_{40}$ secondary phase appear in $Bi_{0.9}Cd_{0.1}FeO_3$ and $Bi_{0.7}Cd_{0.3}FeO_3$ samples, as shown in Figure 1. [41] The impact of Cd-substitution on the lattice parameters and magnetic properties of $BiFeO_3$ can vary depending on the substitution level and other factors, such as temperature and pressure. Generally, Cd-substitution can cause a decrease in the lattice parameters, which results in a decrease in the magnetic properties, as the decrease in lattice parameters can lead to a reduction in the exchange interactions between the magnetic moments in the material. The selenite-type structure is a crystallographic structure that is found in certain types of ferrites. The XRD pattern of ferrite with a silent-type phase typically exhibits characteristic diffraction peaks that can be used to identify the presence of this structure. In Figure 1, the peak between 2theta 25–30 depicts the presence of a selenite-type phase.
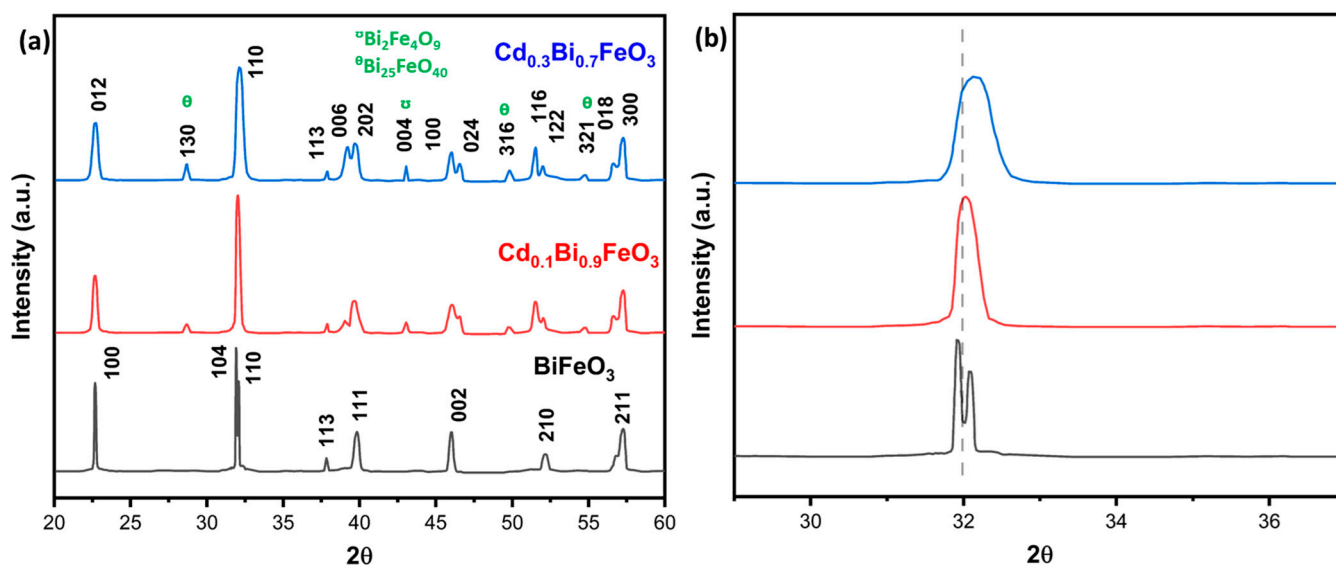
Figure 1. (**a**) XRD patterns of $BiFeO_3$, $Bi_{0.7}Cd_{0.3}FeO_3$, and $Bi_{0.9}Cd_{0.1}FeO_3$ powders calcined at 550 °C, (**b**) zoomed image of the characteristic peak near 32°. The shift towards a higher angle confirms the successful substitution of Cd with Bi in the $BiFeO_3$ crystal.

Debye Scherrer's formula, mentioned in Equation (1), is used to calculate the crystallite size of fabricated materials.

$$D = (k\lambda / \beta \cos \theta) \qquad (1)$$

Here, D represents the crystallite size, k is the shape constant, lambda (λ) is the wavelength of incident X-rays, theta (θ) is the angle of diffraction, and β indicates the full-width half maxima (FWHM) of the characteristic peak under consideration for calculations. The crystalline size of the prepared materials has been shown in Table 1.

Table 1. Crystallite size calculated by the Debye-Scherrer formula.

Material	2θ	hkl	Crystallite Size
$BiFeO_3$	32.17	110	40.62 nm
$Bi_{0.9}Cd_{0.1}FeO_3$	32.06	110	34.97 nm
$Bi_{0.7}Cd_{0.3}FeO_3$	32.01	110	29.14 nm

3.2. Scanning Electron Microscopy

Figure 2 presents the SEM images of $BiFeO_3$, $Bi_{0.9}Cd_{0.1}FeO_3$, and $Bi_{0.7}Cd_{0.3}FeO_3$ powder samples prepared with the chemical co-precipitation method. The SEM images clearly show that the pure $BiFeO_3$ has cubic crystals with a relatively large average particle size of ~0.8 µm. As the concentration of Cd dopant in $BiFeO_3$ is increased, the particle size is considerably decreased. Moreover, a transition from cubic crystals to spherical-shaped particles is observed with Cd doping (Figure 2). The average particle size of $Bi_{0.9}Cd_{0.1}FeO_3$ was calculated to be 0.4 µm with spherical morphology. In the case of $Bi_{0.7}Cd_{0.3}FeO_3$, the particle size was further decreased to ~0.25 µm, while the particles retained their spherical morphology. EDX analysis of $Bi_{0.7}Cd_{0.3}FeO_3$, mentioned in Figure 3, confirms the successful doping of Cd into $BiFeO_3$. It also provides valuable information about the percentage composition of the material. It is worth mentioning that particle size is different from crystallite size determined by XRD analysis mentioned in Table 1. Crystallite size refers to the average size of the crystalline regions in a material, while particle size refers to the size of the individual particles or grains in the material. Crystallite size affects the material's mechanical, optical, and electrical properties, whereas particle size can affect its dispersibility and surface area.
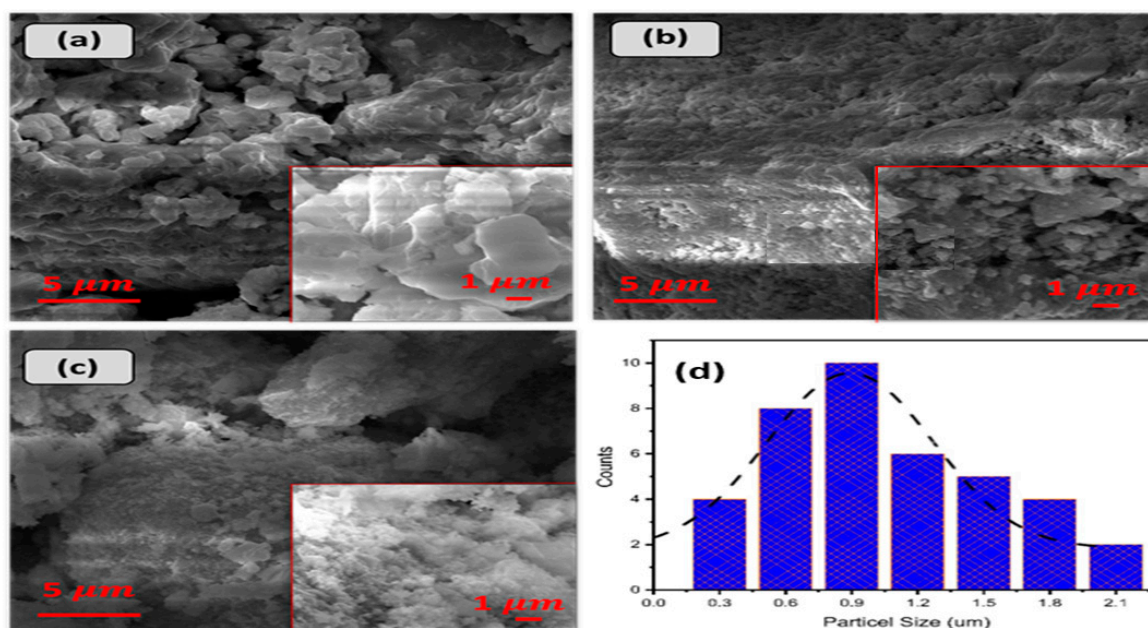
Figure 2. SEM images of (**a**) $BiFeO_3$, (**b**) $Bi_{0.9}Cd_{0.1}FeO_3$, (**c**) $Bi_{0.7}Cd_{0.3}FeO_3$, and (**d**) particle size graph along with Gaussian fitting to evaluate average particle size for a pure sample.
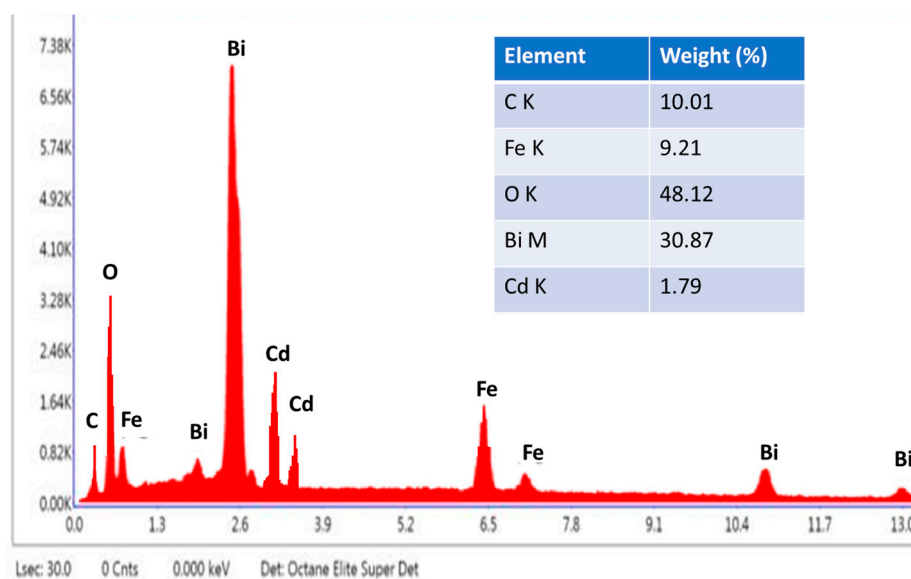

Figure 3. EDX spectrum of $Bi_{0.7}Cd_{0.3}FeO_3$ for elemental compositional analysis confirming the successful doping of Cd into $BiFeO_3$.

3.3. Ultraviolet-Visible Spectroscopy

The UV-Vis spectra of all samples are shown in Figure 4. For $BiFeO_3$, a sharp absorption peak is observed at a wavelength of 360 nm. In Cd-doped samples, the absorption peak is shifted to 395 nm and 420 nm for $Bi_{0.9}Cd_{0.1}FeO_3$ and $Bi_{0.7}Cd_{0.3}FeO_3$, respectively. Figure 4 shows the absorption peak of the prepared samples along with their corresponding Tauc plot. The Tauc plots reveal that the band gaps are direct and the calculated band gap values of $BiFeO_3$, $Bi_{0.9}Cd_{0.1}FeO_3$, and $Bi_{0.7}Cd_{0.3}FeO_3$ are 2.95, 2.76, and 2.51 eV, respectively. It can be inferred from Figure 4 that the band gaps decrease with increasing the doping concentration of Cd in pure $BiFeO_3$, which is evident by the absorption of light in the visible region.
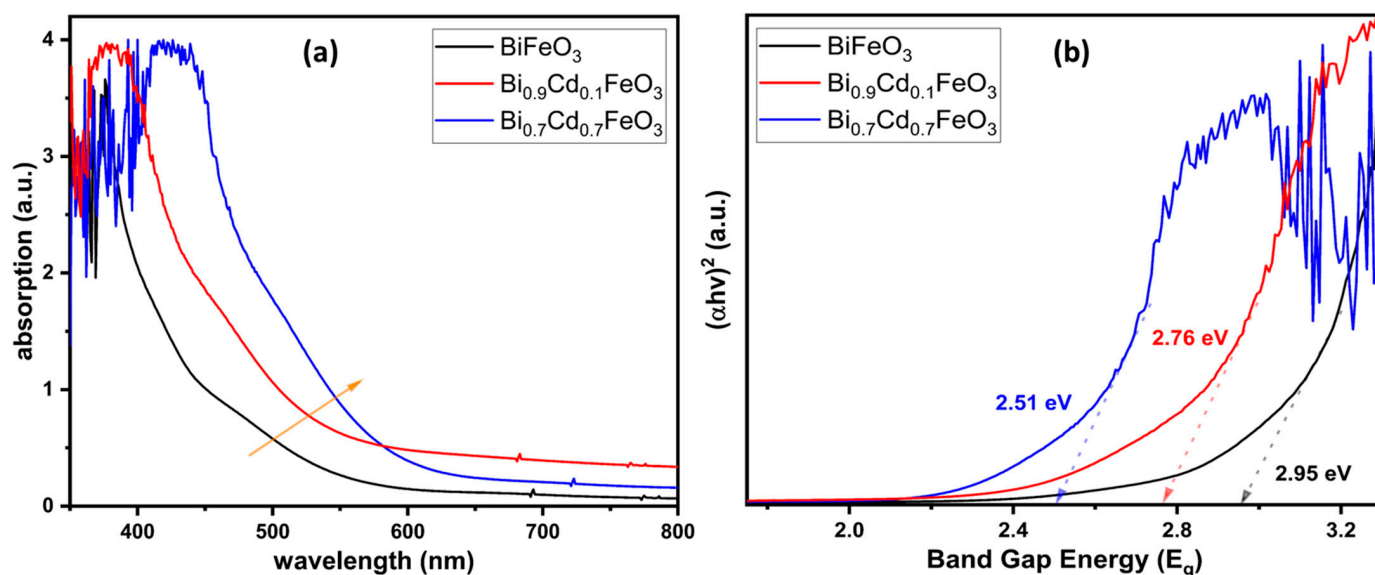
Figure 4. (**a**) UV visible absorption plot for $BiFeO_3$, $Bi_{0.9}Cd_{0.1}O_3$ and $Bi_{0.7}Cd_{0.3}FeO_3$. The arrow in (**a**) shows the increasing pattern of increasing wavelength. (**b**) there corresponding Tauc plot for evaluating the band gap of synthesized samples.

3.4. Fourier Transform Infrared Spectroscopy

To study the oxygen coordination with other metal ions in both A-site and B-site cations in the perovskite structure of all bismuth ferrite samples [42], FT-IR spectroscopy results of the prepared powders are provided in Figure 5. The absorption band is slightly broadened in the range of 3200 cm^{-1} to 3500 cm^{-1}, which might be associated with N-H stretching [43,44]. On some occasions, overlapping of O-H stretching and N-H stretching may also occur. The literature indicates that such types of bands (occurring at 1100 cm^{-1} to 1600 cm^{-1}) are due to the presence of nitrates trapped on the surface [45]. Bands occurring at the very start of the peak, i.e., at 600 cm^{-1}, are found to be the result of the vibrations of Fe-O and Bi-O metal-oxygen bonds [46]. Further, an octahedral FeO_6 group has the characteristic of Fe-O bond bending and stretching vibrations [47–49].
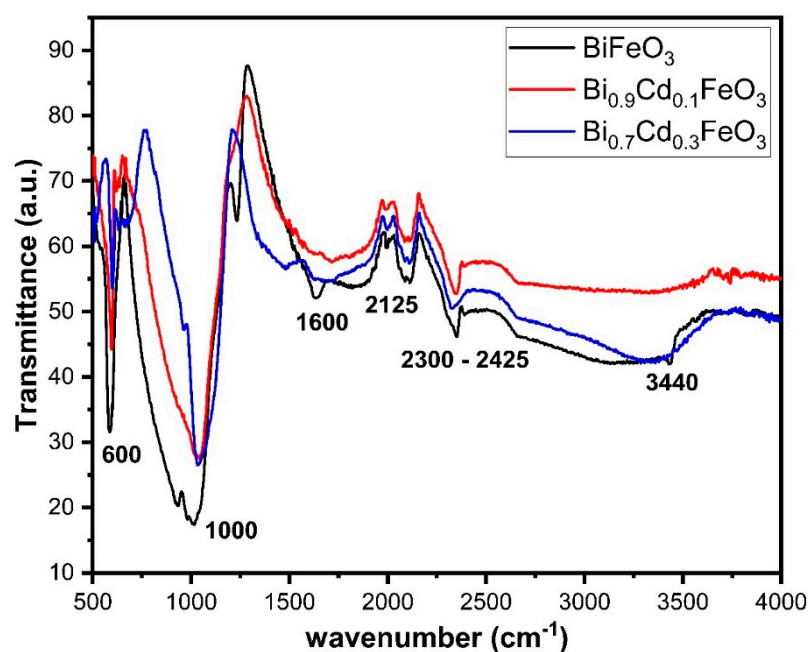

Figure 5. FT-IR spectra of $BiFeO_3$, $Bi_{0.9}Cd_{0.1}FeO_3$, and $Bi_{0.7}Cd_{0.3}FeO_3$.

3.5. Raman Spectroscopy

To study the structural changes concerning the different doping concentrations of Cd in $BiFeO_3$, RS was carried out. This technique is quite sensitive to determining the local symmetrical changes in complex perovskites and ferrites [50]. Figure 6 shows RS spectra of $BiFeO_3$, $Bi_{0.9}Cd_{0.1}FeO_3$, and $Bi_{0.7}Cd_{0.3}FeO_3$ obtained at room temperature. Theoretical group theory study of rhombohedral $BiFeO_3$ (belonging to the R3c space group) suggests 13 Raman modes $4A_1$ and the $9E$ [51]. However, practically, this statement does not hold, since we obtain a relatively small number of Raman modes (due to weak polarization of ions, mode broadening, and expected degeneracy) in the materials having a large number of atoms in their unit cell [52].
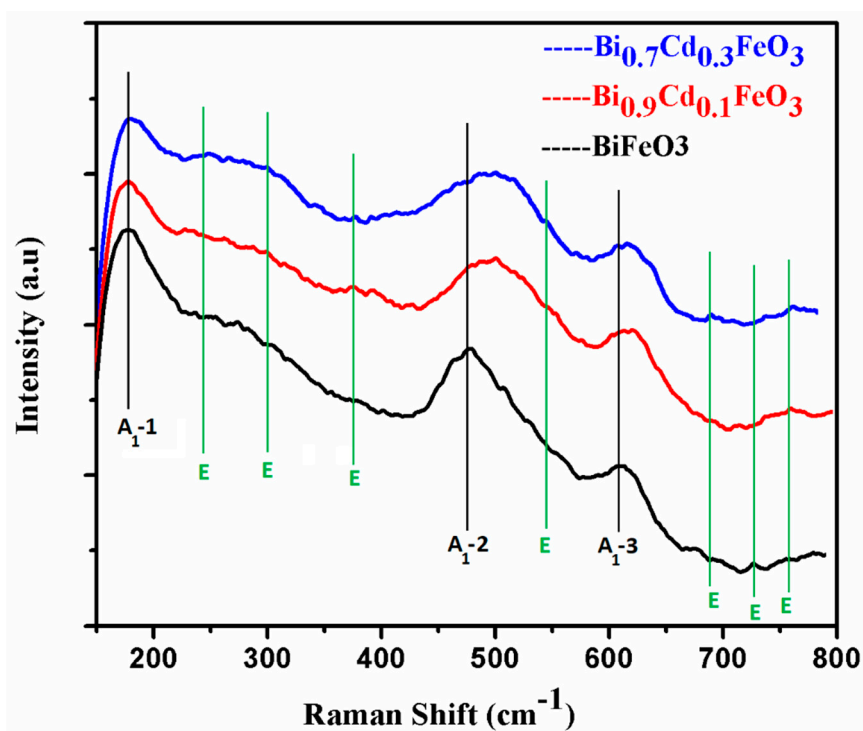

Figure 6. Raman scattering spectra analysis for $BiFeO_3$, $Bi_{0.9}Cd_{0.1}FeO_3$, and $Bi_{0.7}Cd_{0.3}FeO_3$ at room temperature.

For the pure $BiFeO_3$ sample, the A_1-1, A_1-2, and A_1-3 modes (having relatively higher scattering intensity) are observed at 180, 483, and 616 cm^{-1}, respectively. Mode A_1-4 is too weak to be observed. Similarly, all E modes are found to be at 253, 302, 378, 546, 694, 726, and 753 cm^{-1}. As Cd is doped in pure $BiFeO_3$, no remarkable qualitative change in Raman scattering spectra is noticed except that the second and third main A_1 modes are shifted towards the right, i.e., towards the higher order of frequency. The new positions are observed at 501 and 620 cm^{-1}, which seem to be nearly equal for both samples. This is attributed to the fact that Cd has a much lower mass as compared to Bi, indicating that the doping element (Cd) is entering at Bi sites of $BiFeO_3$ [53,54].

The XRD patterns of the sample may show both rhombohedral and orthorhombic phases, while the Raman spectra only detect one of them. This could be because the XRD technique is more sensitive to the long-range ordering of atoms in the sample, while Raman spectroscopy is more sensitive to the bonding of the atoms. The presence of both rhombohedral and orthorhombic phases in the XRD patterns could indicate that the sample contains a mixture of both phases, while Raman spectroscopy is not sensitive enough to detect the small amount of the other phase. It is also possible that the Raman spectra only detect one of the phases because the other phase is in a low concentration and not contributing significantly to the Raman signal.

3.6. Vibrating Sample Magnetometry

To study the magnetic behavior of pure and Cd-doped $BiFeO_3$ samples, VSM was performed with an applied field having a maximum value of 15 kOe at room temperature. Figure 7 shows the M-H curves of $BiFeO_3$, $Bi_{0.9}Cd_{0.1}FeO_3$, and $Bi_{0.7}Cd_{0.3}FeO_3$ samples. It is found that at room temperature, the pure $BiFeO_3$ and Cd-doped $Bi_{0.9}Cd_{0.1}FeO_3$ show very weak ferromagnetic behavior. Interestingly, the obtained result for the bulk $BiFeO_3$ in the present study is quite different when compared with bulk $BiFeO_3$ from the literature, where it has been reported as antiferromagnetic at room temperature [55]. However, for the nano-sized $BiFeO_3$, the literature supports the weak ferromagnetic behavior [56]. This difference in magnetic behavior in bulk and nano-sized $BiFeO_3$ may be due to the reduction of particle size that resulted in no exact compensation of two magnetic sublattices with a unit cell [57]. The size of the particles can affect the magnetic properties of the material. In general, smaller particles have a higher surface-to-volume ratio, which can lead to an increase in the number of defects and impurities and can affect the magnetic properties. In the case of $BiFeO_3$, the magnetic properties are known to be sensitive to particle size and shape, and ferromagnetism has been observed in $BiFeO_3$ nanoparticles.
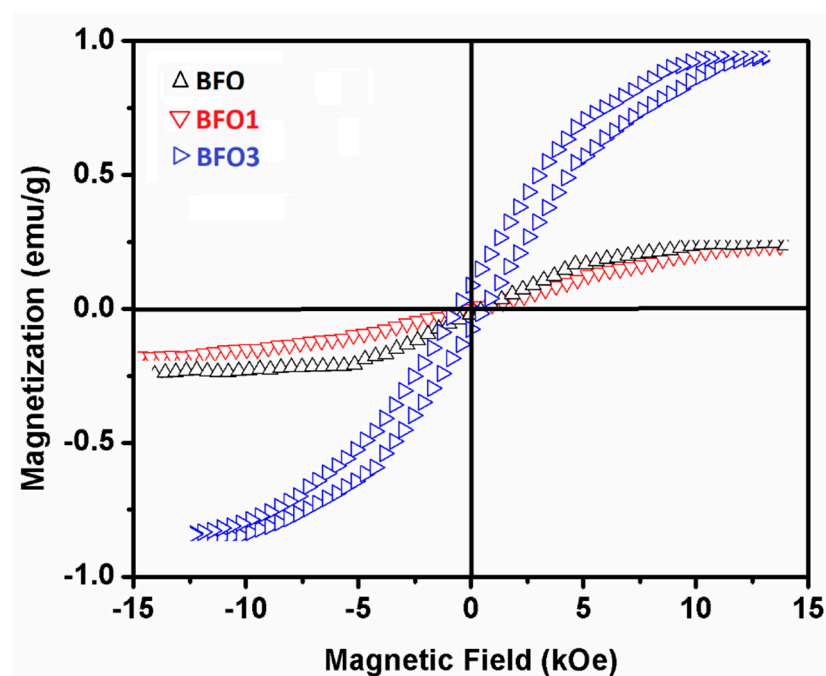

Figure 7. M-H curves of $BiFeO_3$, $Bi_{0.9}Cd_{0.1}FeO_3$, and $Bi_{0.7}Cd_{0.3}FeO_3$ samples at room temperature.

Additionally, the ferromagnetic nature of the M-H loop in $BiFeO_3$ is also related to the presence of Fe ions, which are known to be ferromagnetic. The ferromagnetism in $BiFeO_3$ can also be influenced by other factors, such as the crystal structure, defects, and impurities, as well as the synthesis conditions. Additionally, the result for $Bi_{0.9}Cd_{0.1}FeO_3$ may arise due to the canting of distorted lattice in a previously antiferromagnetically ordered structure, causing an imbalance in antiparallel sublattice magnetization of Fe and Bi ions.

For the doped $Bi_{0.7}Cd_{0.3}FeO_3$ sample, relatively stronger ferromagnetic behavior is observed, which is evident in Figure 6. Further, the measured coercivity (H_c), remnant magnetization (M_r) at maximum (15 kOe) applied external magnetic field are 250 Oe and 0.15 emu/g, respectively. The specific magnetization of $Bi_{0.7}Cd_{0.3}FeO_3$ is calculated to be 0.91 emu/g. The structural transition from rhombohedral to orthorhombic may be the cause of the relatively stronger ferromagnetic behavior of the $Bi_{0.7}Cd_{0.3}FeO_3$ sample. This transition can lead to structural distortion, promoting Fe–Fe atomic interactions and causing an imbalance in magnetic ordering, which otherwise was causing the cancelation of

ferromagnetic behavior. This effect of imbalance in magnetic ordering was not dominant enough to suppress a considerable amount of net ferro-magneticity in $Bi_{0.9}Cd_{0.1}FeO_3$ [58,59].

4. Conclusions

Cd-doped $BiFeO_3$ ($Bi_xCd_{1-x}FeO_3$, x = 0, 0.1, 0.3) samples were successfully synthesized via a simple, facile, and efficient chemical co-precipitation method. A transition from rhombohedral to orthorhombic crystal structure was noticed in the doped samples. The XRD spectra reflected the presence of secondary phases of bismuth ferrite ($Bi_2Fe_4O_9$ and $Bi_{25}FeO_{40}$) in the doped samples. The SEM micrographs revealed that the particle size lies in the range of micrometers. Moreover, the pure $BiFeO_3$ powder showed a cubic shape of crystals, which changed to a spherical shape with doping of Cd. Raman spectroscopy verified the substitution of Cd at Bi sites. FT-IR results confirmed that Cd substitution resulted in bond stretching (due to the difference in radii of Cd and Bi). Further, VSM confirmed very weak ferromagnetic behavior in pure $BiFeO_3$ and Cd-doped $Bi_{0.9}Cd_{0.1}FeO_3$, while relatively stronger ferromagnetic behavior was observed for $Bi_{0.7}Cd_{0.3}FeO_3$ because the reduction in particle size enhances the magnetic ferromagnetic behavior of the material. For $Bi_{0.7}Cd_{0.3}FeO_3$, the measured coercivity (H_c) remnant magnetization (M_r), at maximum, applied external magnetic field, were 250 Oe and 0.15 emu/g, respectively.

Author Contributions: Conceptualization, S.Z.M.; methodology, S.Z.M.; software, M.A.; validation, F.M.A. and S.M.E.; formal analysis, A.M.G. and F.M.A.; investigation, M.A.; resources, S.Z.M.; data curation, S.M.E.; writing—original draft preparation, S.Z.M.; writing—review and editing, M.A.; visualization, S.Z.M.; supervision, S.Z.M. and M.A.; project administration, A.M.G. and S.M.E.; funding acquisition, A.M.G. and S.M.E. All authors have read and agreed to the published version of the manuscript.

Institutional Review Board Statement: Not applicable.

Informed Consent Statement: Not applicable.

Data Availability Statement: Not applicable.

Conflicts of Interest: The authors declare no conflict of interest.

References

1. Wang, J.B.N.J.; Neaton, J.B.; Zheng, H.; Nagarajan, V.; Ogale, S.B.; Liu, B.; Viehland, D.; Vaithyanathan, V.; Schlom, D.G.; Waghmare, U.V.; et al. Epitaxial $BiFeO_3$ multiferroic thin film heterostructures. *Science* **2003**, *299*, 1719–1722. [CrossRef] [PubMed]
2. Catalan, G.; Scott, J.F. Physics and applications of bismuth ferrite. *Adv. Mater.* **2009**, *21*, 2463–2485. [CrossRef]
3. Arshad, M.; Hassan, A.; Haider, Q.; Alharbi, F.M.; Alsubaie, N.; Alhushaybari, A.; Burduhos-Nergis, D.-P.; Galal, A.M. Rotating Hybrid Nanofluid Flow with Chemical Reaction and Thermal Radiation between Parallel Plates. *Nanomaterials* **2022**, *12*, 4177. [CrossRef]
4. Eerenstein, W.; Mathur, N.D.; Scott, J.F. Multiferroic and magnetoelectric materials. *Nature* **2006**, *442*, 759–765. [CrossRef] [PubMed]
5. Dhanalakshmi, B.; Pratap, K.; Rao, B.P.; Rao, P.S. Effects of Mn doping on structural, dielectric, and multiferroic properties of $BiFeO_3$ nanoceramics. *J. Alloys Compd.* **2016**, *676*, 193–201. [CrossRef]
6. Dong, S.; Cheng, J.; Li, J.F.; Viehland, D. Enhanced magnetoelectric effects in laminate composites of Terfenol-D/Pb (Zr, Ti) O_3 under resonant drive. *Appl. Phys. Lett.* **2003**, *83*, 4812–4814. [CrossRef]
7. Fischer, P.; Polomska, M.; Sosnowska, I.; Szymanski, M. Temperature dependence of the crystal and magnetic structures of $BiFeO_3$. *J. Phys. C Solid State Phys.* **1980**, *13*, 1931. [CrossRef]
8. Dzik, J.; Feliksik, K.; Pikula, T.; Panek, R.; Rerak, M. Influence of Dy doping on the properties of $BiFeO_3$. *Arch. Metall. Mater.* **2018**, *63*, 1351–1355.
9. Ishaq, B.; Murtaza, G.; Sharif, S.; Khan, M.A.; Akhtar, N.; Will, I.; Saleem, M.; Ramay, S.M. Investigating the effect of Cd-Mn co-doped nano-sized $BiFeO_3$ on its physical properties. *Results Phys.* **2016**, *6*, 675–682. [CrossRef]
10. Karpinsky, D.; Silibin, M.; Trukhanov, A.; Zhaludkevich, A.; Maniecki, T.; Maniukiewicz, W.; Sikolenko, V.; Paixão, J.; Khomchenko, V. A correlation between crystal structure and magnetic properties in co-doped $BiFeO_3$ ceramics. *J. Phys. Chem. Solids* **2019**, *126*, 164–169. [CrossRef]
11. Arafat, S.S. Structural transition and magnetic properties of high Cr-doped $BiFeO_3$ ceramic. *Cerâmica* **2020**, *66*, 114–118. [CrossRef]

12. Zhuang, J.; Zhao, J.; Su, L.W.; Wu, H.; Bokov, A.A.; Ren, W.; Ye, Z.G. Structure and local polar domains of Dy-modified $BiFeO_3$–$PbTiO_3$ multiferroic solid solutions. *J. Mater. Chem. C* **2015**, *3*, 12450–12456. [CrossRef]

13. Arshad, M.; Hussain, A.; Hassan, A.; Karamti, H.; Wroblewski, P.; Khan, I.; Andualem, M.; Galal, A.M. Scrutinization of Slip Due to Lateral Velocity on the Dynamics of Engine Oil Conveying Cupric and Alumina Nanoparticles Subject to Coriolis Force. *Math. Probl. Eng.* **2022**, *2022*, 2526951. [CrossRef]

14. Teague, J.R.; Gerson, R.; James, W.J. Dielectric hysteresis in single crystal $BiFeO_3$. *Solid State Commun.* **1970**, *8*, 1073–1074. [CrossRef]

15. Carvalho, T.T.; Tavares, P.B. Synthesis and thermodynamic stability of multiferroic $BiFeO_3$. *Mater. Lett.* **2008**, *62*, 3984–3986. [CrossRef]

16. Zhou, W.; Deng, H.; Yu, L.; Yang, P.; Chu, J. Band-gap narrowing and magnetic behavior of Ni-doped Ba $(Ti_{0.875}Ce_{0.125})$ O_3 thin films. *J. Phys. D Appl. Phys.* **2015**, *48*, 455308. [CrossRef]

17. Arshad, M.; Karamti, H.; Awrejcewicz, J.; Grzelczyk, D.; Galal, A.M. Thermal Transmission Comparison of Nanofluids over Stretching Surface under the Influence of Magnetic Field. *Micromachines* **2022**, *13*, 1296. [CrossRef]

18. Yuan, G.L.; Or, S.W.; Liu, J.M.; Liu, Z.G. Structural transformation and ferroelectromagnetic behavior in single-phase $Bi_{1−x}Nd_xFeO_3$ multiferroic ceramics. *Appl. Phys. Lett.* **2006**, *89*, 052905. [CrossRef]

19. Yuan, G.L.; Or, S.W.; Chan, H.L.W. Structural transformation and ferroelectric–paraelectric phase transition in $Bi_{1−x}La_xFeO_3$ (x = 0–0.25) multiferroic ceramics. *J. Phys. D Appl. Phys.* **2007**, *40*, 1196. [CrossRef]

20. Khomchenko, V.A.; Kiselev, D.A.; Selezneva, E.K.; Vieira, J.M.; Lopes, A.M.L.; Pogorelov, Y.G.; Araujo, J.P.; Kholkin, A.L. Weak ferromagnetism in diamagnetically-doped $Bi_{1−x}A_xFeO_3$ (A = Ca, Sr, Pb, Ba) multiferroics. *Mater. Lett.* **2008**, *62*, 1927–1929. [CrossRef]

21. Reddy, V.A.; Pathak, N.P.; Nath, R. Domain switching in spray pyrolysis-deposited nano-crystalline $BiFeO_3$ films. *Phys. Scr.* **2012**, *86*, 065701. [CrossRef]

22. Park, T.J.; Papaefthymiou, G.C.; Viescas, A.J.; Lee, Y.; Zhou, H.; Wong, S.S. Composition-dependent magnetic properties of $BiFeO_3$-$BaTiO_3$ solid solution nanostructures. *Phys. Rev. B* **2010**, *82*, 024431. [CrossRef]

23. Chaudhuri, A.; Mandal, K. Enhancement of Ferromagnetic and Dielectric properties of nanostructured Barium doped Bismuth Ferrite fabricated by facile hydrothermal route. In *AIP Conference Proceedings*; AIP Publishing LLC: Melville, NY, USA, 2015; Volume 1665, p. 050022.

24. Tagantsev, A.K.; Stolichnov, I.; Colla, E.L.; Setter, N. Polarization fatigue in ferroelectric films: Basic experimental findings, phenomenological scenarios, and microscopic features. *J. Appl. Phys.* **2001**, *90*, 1387–1402. [CrossRef]

25. Kumar, M.; Yadav, K.L. Study of room temperature magnetoelectric coupling in Ti substituted bismuth ferrite system. *J. Appl. Phys.* **2006**, *100*, 074111. [CrossRef]

26. Qi, X.; Dho, J.; Tomov, R.; Blamire, M.G.; MacManus-Driscoll, J.L. Greatly reduced leakage current and conduction mechanism in aliovalent-ion-doped $BiFeO_3$. *Appl. Phys. Lett.* **2005**, *86*, 062903. [CrossRef]

27. Tabares-Munoz, C.; Rivera, J.P.; Bezinges, A.; Monnier, A.; Schmid, H. Measurement of the quadratic magnetoelectric effect on single crystalline $BiFeO_3$. *Jpn. J. Appl. Phys.* **1985**, *24*, 1051. [CrossRef]

28. Przenioslo, R.; Regulski, M.; Sosnowska, I. Modulation in multiferroic $BiFeO_3$: Cycloidal, elliptical, or SDW? *J. Phys. Soc. Jpn.* **2006**, *75*, 084718. [CrossRef]

29. Sosnowska, I.; Neumaier, T.P.; Steichele, E. Spiral magnetic ordering in bismuth ferrite. *J. Phys. C Solid State Phys.* **1982**, *15*, 4835. [CrossRef]

30. Maurya, D.; Thota, H.; Nalwa, K.S.; Garg, A. $BiFeO_3$ ceramics synthesized by mechanical activation assisted versus conventional solid-state-reaction process: A comparative study. *J. Alloys Compd.* **2009**, *477*, 780–784. [CrossRef]

31. Ghosh, S.; Dasgupta, S.; Sen, A.; Maiti, H.S. Low temperature synthesis of bismuth ferrite nanoparticles by a ferrioxalate precursor method. *Mater. Res. Bull.* **2005**, *40*, 2073–2079. [CrossRef]

32. Cho, C.M.; Noh, J.H.; Cho, I.S.; An, J.S.; Hong, K.S.; Kim, J.Y. Low-temperature hydrothermal synthesis of pure $BiFeO_3$ nanopowders using triethanolamine and their applications as visible-light photocatalysts. *J. Am. Ceram. Soc.* **2008**, *91*, 3753–3755. [CrossRef]

33. Park, T.J.; Papaefthymiou, G.C.; Viescas, A.J.; Moodenbaugh, A.R.; Wong, S.S. Size-dependent magnetic properties of single-crystalline multiferroic $BiFeO_3$ nanoparticles. *Nano Lett.* **2007**, *7*, 766–772. [CrossRef] [PubMed]

34. Yu, B.; Li, M.; Liu, J.; Guo, D.; Pei, L.; Zhao, X. Effects of ion doping at different sites on electrical properties of multiferroic $BiFeO_3$ ceramics. *J. Phys. D Appl. Phys.* **2008**, *41*, 065003. [CrossRef]

35. Hassan, A.; Hussain, A.; Fernandez-Gamiz, U.; Arshad, M.; Karamti, H.; Awrejcewicz, J.; Alharbi, F.M.; Elfasakhany, A.; Galal, A.M. Computational investigation of magneto-hydrodynamic flow of newtonian fluid behavior over obstacles placed in rectangular cavity. *Alex. Eng. J.* **2023**, *65*, 163–188. [CrossRef]

36. Kim, J.K.; Kim, S.S.; Kim, W.J. Sol–gel synthesis and properties of multiferroic $BiFeO_3$. *Mater. Lett.* **2005**, *59*, 4006–4009. [CrossRef]

37. Han, J.; Huang, Y.-H.; Wu, X.-J.; Wu, C.-L.; Wei, W.; Peng, B.; Huang, W.; Goodenough, J.B. Tunable synthesis of bismuth ferrites with various morphologies. *Adv. Mater.* **2006**, *18*, 2145–2148. [CrossRef]

38. Arshad, M.; Hussain, A.; Elfasakhany, A.; Gouadria, S.; Awrejcewicz, J.; Pawłowski, W.; Elkotb, M.A.; Alharbi, F.M. Magneto-hydrodynamic flow above exponentially stretchable surface with chemical reaction. *Symmetry* **2022**, *14*, 1688. [CrossRef]

39. Chen, C.; Cheng, J.; Yu, S.; Che, L.; Meng, Z. Hydrothermal synthesis of perovskite bismuth ferrite crystallites. *J. Cryst. Growth* **2006**, *291*, 135–139. [CrossRef]

40. Özdemir, D.K. Temperature Susceptibility and Rheological Aging Characteristics of the Bitumen Having Different Penetration Grades. *Black Sea J. Eng. Sci.* **2021**, *4*, 209–213.

41. Cheng, Z.; Li, A.H.; Wang, X.L.; Dou, S.X.; Ozawa, K.; Kimura, H.; Zhang, S.; Shrout, T.R. Structure, ferroelectric properties, and magnetic properties of the La-doped bismuth ferrite. *J. Appl. Phys.* **2008**, *103*, 07E507. [CrossRef]

42. Pradeep, A.; Chandrasekaran, G. FTIR study of Ni, Cu and Zn substituted nano-particles of $MgFe_2O_4$. *Mater. Lett.* **2006**, *60*, 371–374. [CrossRef]

43. Muneeswaran, M.; Jegatheesan, P.; Giridharan, N.V. Synthesis of nanosized $BiFeO_3$ powders by co-precipitation method. *J. Exp. Nanosci.* **2013**, *8*, 341–346. [CrossRef]

44. Parikh, A.; Madamwar, D. Partial characterization of extracellular polysaccharides from cyanobacteria. *Bioresour. Technol.* **2006**, *97*, 1822–1827. [CrossRef] [PubMed]

45. Ghosh, S.; Dasgupta, S.; Sen, A.; Sekhar Maiti, H. Low-temperature synthesis of nanosized bismuth ferrite by soft chemical route. *J. Am. Ceram. Soc.* **2005**, *88*, 1349–1352. [CrossRef]

46. Nakanishi, K.; Solomon, P.H. *Infrared Absorption Spectroscopy*; Holden-day: Eads, TN, USA, 1977.

47. Anthony Raj, C.; Muneeswaran, M.; Jegatheesan, P.; Giridharan, N.V.; Sivakumar, V.; Senguttuvan, G. Effect of annealing time in the low-temperature growth of BFO thin films spin coated on glass substrates. *J. Mater. Sci. Mater. Electron.* **2013**, *24*, 4148–4154. [CrossRef]

48. Biasotto, G.; Simões, A.Z.; Foschini, C.R.; Zaghete, M.A.; Varela, J.A.; Longo, E. Microwave-hydrothermal synthesis of perovskite bismuth ferrite nanoparticles. *Mater. Res. Bull.* **2011**, *46*, 2543–2547. [CrossRef]

49. Yotburut, B.; Yamwong, T.; Thongbai, P.; Maensiri, S. Synthesis and characterization of coprecipitation-prepared La-doped $BiFeO_3$ nanopowders and their bulk dielectric properties. *Jpn. J. Appl. Phys.* **2014**, *53*, 06JG13. [CrossRef]

50. Arshad, M.; Hassan, A. A numerical study on the hybrid nanofluid flow between a permeable rotating system. *Eur. Phys. J. Plus* **2022**, *137*, 1126. [CrossRef]

51. Haumont, R.; Kreisel, J.; Bouvier, P. Raman scattering of the model multiferroic oxide $BiFeO_3$: Effect of temperature, pressure and stress. *Phase Transit.* **2006**, *79*, 1043–1064. [CrossRef]

52. White, W.B. Structure of particles and the structure of crystals: Information from vibrational spectroscopy. *J. Ceram. Process. Res.* **2005**, *6*, 1–9.

53. Hassan, A.; Hussain, A.; Arshad, M.; Awrejcewicz, J.; Pawlowski, W.; Alharbi, F.M.; Karamti, H. Heat and mass transport analysis of MHD rotating hybrid nanofluids conveying silver and molybdenum di-sulfide nano-particles under effect of linear and non-linear radiation. *Energies* **2022**, *15*, 6269. [CrossRef]

54. Bozgeyik, M.S.; Katiyar, R.K.; Katiyar, R.S. Improved magnetic properties of bismuth ferrite ceramics by La and Gd co-substitution. *J. Electroceram.* **2018**, *40*, 247–256. [CrossRef]

55. Zhang, S.T.; Lu, M.H.; Wu, D.; Chen, Y.F.; Ming, N.B. Larger polarization and weak ferromagnetism in quenched $BiFeO_3$ ceramics with a distorted rhombohedral crystal structure. *Appl. Phys. Lett.* **2005**, *87*, 262907. [CrossRef]

56. Sinha, A.; Bhushan, B.; Jagannath; Sharma, R.; Sen, S.; Mandal, B.; Meena, S.; Bhatt, P.; Prajapat, C.; Priyam, A.; et al. Enhanced dielectric, magnetic and optical properties of Cr-doped $BiFeO_3$ multiferroic nanoparticles synthesized by sol-gel route. *Results Phys.* **2019**, *13*, 102299. [CrossRef]

57. Dutta, D.P.; Mandal, B.P.; Naik, R.; Lawes, G.; Tyagi, A.K. Magnetic, ferroelectric, and magnetocapacitive properties of sonochemically synthesized Sc-doped $BiFeO_3$ nanoparticles. *J. Phys. Chem. C* **2013**, *117*, 2382–2389. [CrossRef]

58. Moriya, T. Anisotropic superexchange interaction and weak ferromagnetism. *Phys. Rev.* **1960**, *120*, 91. [CrossRef]

59. Pradhan, S.K.; Roul, B.K.; Sahu, D.R. Enhancement of ferromagnetism and multiferroicity in Ho doped Fe rich $BiFeO_3$. *Solid State Commun.* **2012**, *152*, 1176–1180. [CrossRef]